arXiv:1603.01492v2 [cond-mat.supr-con] 19 Aug 2016

Charge induced nematicity in FeSe

Pierre Massat,[1] Donato Farina,[1] Indranil Paul,[1] Sandra Karlsson,[2] Pierre Strobel,[2] Pierre Toulemonde,[2] Marie-Aude Méasson,[1] Maximilien Cazayous,[1] Alain Sacuto,[1] Shigeru Kasahara,[3] Takasada Shibauchi,[4] Yuji Matsuda,[3] and Yann Gallais[1,*]

[1]*Laboratoire Matériaux et Phénomènes Quantiques, UMR 7162 CNRS, Université Paris Diderot, Bat. Condorcet 75205 Paris Cedex 13, France*
[2]*Institut Néél, CNRS UPR2940 and Université Grenoble Alpes, 38042 Grenoble, France*
[3]*Department of Physics, Kyoto University, Kyoto 606-8502, Japan*
[4]*Department of Advanced Materials Science, University of Tokyo, Kashiwa, Chiba 277-8561, Japan*

(Dated: August 22, 2016)

The spontaneous appearance of nematicity, a state of matter that breaks rotation but not translation symmetry, is one of the most intriguing property of the iron based superconductors (Fe SC), and has relevance for the cuprates as well. Establishing the critical electronic modes behind nematicity remains however a challenge, because their associated susceptibilities are not easily accessible by conventional probes. Here using FeSe as a model system, and symmetry resolved electronic Raman scattering as a probe, we unravel the presence of critical charge nematic fluctuations near the structural / nematic transition temperature, $T_S \sim 90$ K. The diverging behavior of the associated nematic susceptibility foretells the presence of a Pomeranchuk instability of the Fermi surface with d-wave symmetry. The excellent scaling between the observed nematic susceptibility and elastic modulus data demonstrates that the structural distortion is driven by this d-wave Pomeranchuk transition. Our results make a strong case for charge induced nematicity in FeSe.

Electronic nematicity, whereby electrons break rotational symmetry spontaneously, is a ubiquitous property of the iron-based superconductors (Fe SC) [1]. As it is often accompanied by magnetic order, an established route to nematicity is via critical magnetic fluctuations [2]. However, this mechanism has been questionned in the iron-chalcogenide FeSe, where the nematic transition occurs without magnetic order, indicating a different paradigm for nematicity [3–5, 8].

Despite its simple crystallographic structure, FeSe displays remarkable properties. Its superconducting transition temperature T_c is relatively low at ambient pressure ($\sim$9 K), but it reaches up to 37 K upon applying hydrostatic pressure [7, 8]. Its Fermi energy is small [2, 10–12], and in the normal state it shows bad metal behavior [2, 13]. Its nematic properties are peculiar as well. The lattice distortion, elastic softening and elasto-resistvity measurements associated with the structural transition at $T_S \sim 90$ K are comparable with other Fe SC [3, 8, 11], yet Nuclear Magnetic Resonance (NMR) and inelastic neutron scattering measurements do not detect sizable low energy spin fluctuations above T_S [4, 8, 14], putting into question the spin nematic scenario envisaged in other Fe SC [2]. While it has been argued that the magnetic scenario may still apply [15–19], there is growing interest in alternative scenario where charge or orbital degrees of freedom play a more pre-dominant role than spins [5, 11, 20, 21]. However, until now direct experimental observation of critical fluctuations associated with electronic charge or orbital nematicity in the tetragonal phase was lacking.

Here, we investigate the nature of nematicity in FeSe by using the unique ability of electronic Raman scattering to selectively probe the dynamics of electronic nematic degrees of freedom free from lattice effects [5–7, 22, 24, 26]. We unravel the presence of critical charge nematic fluctuations in the tetragonal phase which signals the presence of a d-wave Pomeranchuk instability of the Fermi surface [28]. The extracted nematic susceptibility shows quantitative scaling with the measured lattice softening [8, 10], demonstrating that charge nematic fluctuations account entirely for the lattice instability. Our results make a strong case for itinerant electronic charge driven nematicity in FeSe.

Raman scattering is a photon-in photon-out process, whereby a monochromatic visible light is inelastically scattered at a different frequency by dynamical fluctuations of the electrical polarizability of the sample (Fig. 1(a)). In metals the Raman spectra at low frequency shifts are typically composed of sharp optical phonon peaks super-imposed on a broad electronic background, generally referred to as electronic Raman scattering (ERS). The ERS intensity measures the long wavelength dynamical charge correlation function in the symmetry channel μ: $S_\mu(\omega) \equiv \langle \rho^\dagger_\mu(\omega)\rho_\mu(\omega)\rangle$, where ω is the frequency (or Raman) shift between incoming and scattered photons and ρ_μ is the form factor weighted electronic charge [30]. The fluctuation-dissipation theorem in turn links the measured correlation function S_μ to the imaginary part of the Raman response function χ''_μ: $S_\mu(\omega) = \frac{1}{\pi}[1 + n_B(\omega, T)]\chi''_\mu(\omega)$, where n_B is the Bose function.

Being a symmetry resolved probe of the charge fluctuation dynamics with zero momentum transfer, electronic Raman scattering is ideally suited to detect critical in plane charge nematic fluctuations [5, 22]. The symme-

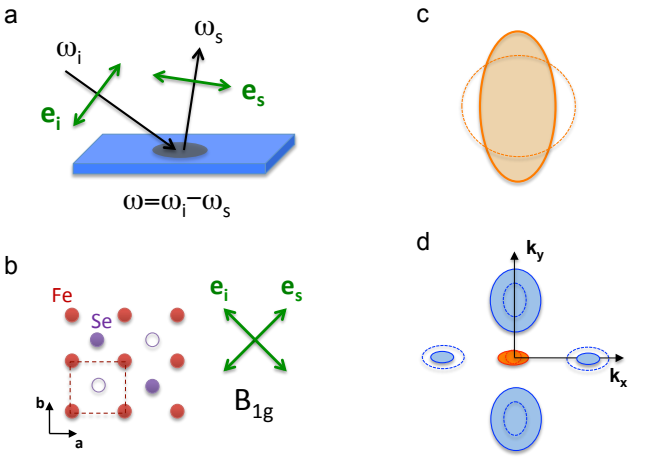

FIG. 1: (a) Schematic of the Raman scattering process with incoming and scattered photons of frequency $\omega_{i/s}$ and polarization $\mathbf{e}_{i/s}$ respectively. The Raman shift is defined as the frequency shift between the incoming and scattered photon frequencies (b) FeSe ab plane with Se atoms alternating above and below the plane defined by the Fe atoms. The 1 Fe unit cell, which neglects the alternating Se atoms, is drawn in dotted lines. In the tetragonal phase above T_S, a=b and the crystal structure of FeSe has a fourfold symmetry axis. The B_{1g} symmetry is obtained using crossed incoming and scattered photon polarizations at 45 degrees of the Fe-Fe bonds. (c)-(d) Fermi surface deformation associated to a d-wave Pomeranchuk order for (c) an isotropic Fermi liquid and (d) the multiband Fe SC showing d-wave like deformations with global B_{1g} symmetry which break the fourfold symmetry axis. The deformations shown are consistent with angle resolved photoemission spectroscopy (ARPES) measurements in the orthorhombic phase of FeSe [32]: while the hole pocket (red) expand along one direction, the elliptical electron pockets (blue) shrink (expand) along the same (other) direction. The 1 Fe unit cell is used.

try of the charge fluctuations μ probed in a Raman experiment is fixed by the directions of the incoming and scattered photon polarizations. Of interest here is the B_{1g} symmetry (using 1 Fe/cell notation, see Fig. 1(b)), obtained for photons polarized along the diagonals of the Fe-Fe bonds and which transforms as k_x^2-k_y^2. The B_{1g} charge nematic fluctuations probed by Raman are equivalent to a Fermi surface deformation with d-wave symmetry. This electronic instability was predicted by Pomeranchuk to occur in an isotropic Fermi liquid in which the Fermi surface spontaneously deforms along a specific direction, breaking rotational symmetry [28] (see Fig. 1(c)). In the context of Fe SC the B_{1g} Raman response probes the fluctuations associated to a multiband version of a d-wave Pomeranchuk order parameter which breaks the fourfold symmetry axis (Fig. 1(d)): $\rho_{B_{1g}} = \sum_{k,\alpha} f_k n_{k,\alpha}$ where α is the orbital index, f_k a d-wave form factor which transforms as k_x^2-k_y^2 and n_k the electron density [6].

Raman scattering experiments were performed on two different FeSe crystals (SP208 and MK, see Supplemental Material and [1, 32]). Figure 2(a) displays the Raman response χ''_μ in different symmetries μ as a function of temperature in the tetragonal phase ($T > T_S$) for SP208. For comparison besides the response in B_{1g} symmetry, we also show the response in B_{2g} and A_{1g} symmetries which transform as $k_x k_y$ and $k_x^2+k_y^2$ respectively (see form factors in the insets of Fig. 2(a)). Upon cooling the $\mu = B_{1g}$ Raman response displays an overall enhancement over a wide energy range extending up to 2000 cm^{-1}. At high temperature the response is dominated by a broad peak, centered around 400 cm^{-1} and whose weight increases on cooling. In addition a relatively sharp peak emerges below 100 cm^{-1}: it softens and gains considerably in intensity upon approaching T_S (Fig. 2(b)). By contrast, the response in the two other configurations is only mildly temperature dependent. The B_{2g} response shows a weak suppression above 500 cm^{-1} and a build-up of spectral weight between 200 and 250 cm^{-1}, which likely originates from an interband transition between nearly parallel spin-orbit split hole bands at the Γ point [11, 33]. Below T_S the B_{1g} response strongly reconstructs (Fig. 2(c)): the low energy response is suppressed and there is a weak transfer of spectral weight at higher energy, above 500 cm^{-1}, in agreement with a previous Raman study [34]. Below T_c superconducting gaps open on the different Fermi pockets (inset of Fig. 2(c)) giving rise to two sharp peaks at 2Δ=28 ($\pm$1) cm^{-1} ($\sim$3.5 meV) and 37 ($\pm$2) cm^{-1} ($\sim$4.6 meV), in broad agreement with Scanning Tunneling Microscopy (STM) measurements [2].

Focusing on the tetragonal phase, we use the fact that the Raman responses at finite frequency can be translated into their corresponding symmetry resolved charge susceptibilities at zero-frequency using the Kramers-Kronig relation,

$$\chi_\mu(T) = \frac{2}{\pi}\int_0^\Lambda \frac{\chi''_\mu(T,\omega)}{\omega} d\omega. \qquad (1)$$

The susceptibilities obtained by integrating the finite frequency responses up to $\Lambda = 2000\ cm^{-1}$ are shown as a function of temperature in Fig. 3. While the B_{2g} and A_{1g} susceptibilities are nearly T-independent, the B_{1g} susceptibility $\chi_{B_{1g}}$ shows a strong enhancement with lowering temperature and subsequently collapses below T_S. This demonstrates the growth of charge nematic fluctuations in the tetragonal phase which are arrested by the structural transition at T_S. For both SP208 and MK crystals the temperature dependence of $\chi_{B_{1g}}$ above T_S is well captured by a Curie-Weiss law $\chi_{B_{1g}}(T) = \frac{B}{T-T_0}$, with a Curie-Weiss temperature T_0 significantly below T_S, namely 8 K and 20 K for SP208 and MK respectively.

A key step in the data interpretation is that the nematic fluctuations described above are entirely electronic in origin, and are not affected by the fluctuations of the orthorhombic strain $u_{xx} - u_{yy}$, where $\hat{u}$ is the lattice

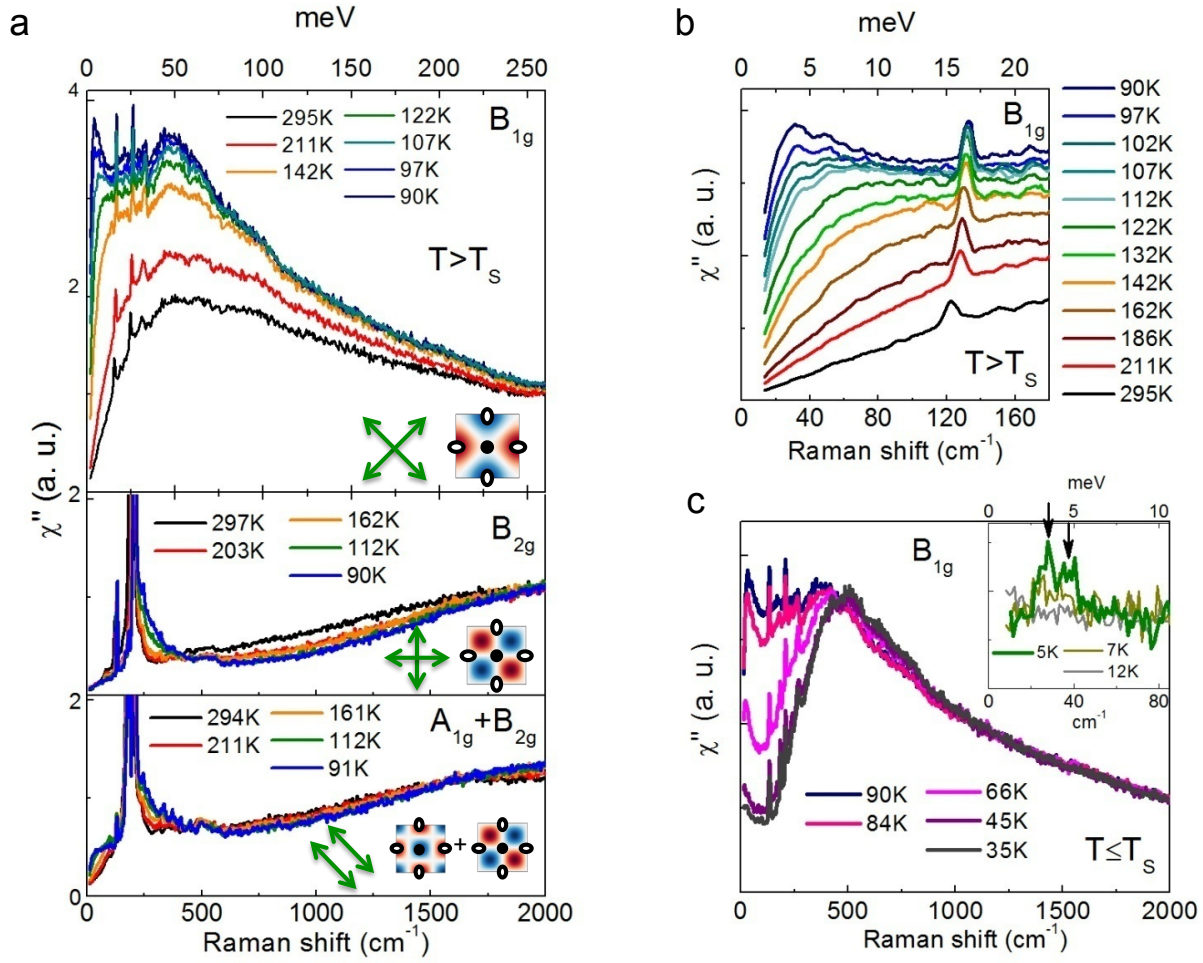

FIG. 2: (a) Symmetry dependent Raman spectra of FeSe (SP208 crystal) above T_S=87 K using 2.33 eV photons. The sharp peaks super-imposed on the electronic continuum are due to Raman active optical phonons. Also shown in inset are the schematics k-space structures of the Raman form factors in different symmetries (blue and red colors indicate positive and negative amplitudes respectively), and the polarization configurations used to select them. (b) Temperature dependence of the low energy B_{1g} spectra above T_S. (c) Evolution of the B_{1g} spectra accross T_S. The inset shows the spectra across the superconducting transition at T_c=8.5 K (SP208). The arrows indicate 2Δ superconducting peaks.

strain tensor [6]. The lattice fluctuations are coupled to the electronic Pomeranchuk order parameter $\rho_{B_{1g}}$ via the electron-phonon interaction $\mathcal{H}_{\rm el-ph} = \lambda\rho_{B_{1g}}(u_{xx} - u_{yy})$, where λ is the coupling constant. The full, measured nematic susceptibility at momentum $\mathbf{q}$ along the relevant high-symmetry direction and frequency ω can be expressed as

$$(\chi_{B_{1g}})^{-1}(\mathbf{q},\omega) = (\chi^0_{B_{1g}})^{-1}(\mathbf{q},\omega) - \frac{\lambda^2 q^2}{C^0_S q^2 - \omega^2}. \quad (2)$$

Here $\chi^0_{B_{1g}}(\mathbf{q},\omega)$ is the electronic susceptibility associated with $\rho_{B_{1g}}$ in the absence of the lattice, and the second term is the contribution of the orthorhombic strain with the elastic shear modulus C^0_S. Crucially, the nematic susceptibility obtained from the finite frequency Raman spectra ($\omega > 8$ cm^{-1}) using Eq. (1) is in the dynamical limit, i.e., $\chi_\mu(T) = \lim_{\omega\to 0}\chi_\mu(T,\omega,q=0)$. In this limit the second term of Eq. (2) vanishes, implying that the extracted nematic susceptibility does not couple to the orthorhombic strain fluctuations [6, 24, 35] and, therefore, T_0 represents the bare electronic charge nematic transition temperature that is un-renormalized by the lattice. We conclude that the observed Curie-Weiss behavior demonstrates the presence of a d-wave Pomeranchuk instability of purely electronic origin in FeSe. This is in agreement with a recent renormalization group analysis, which shows that the leading instability is in the Pomeranchuk channel in low Fermi energy systems like FeSe [36]. The d-wave Pomeranchuk order may explain the peculiar k-dependent orbital splitting observed by angle resolved photoemission spectroscopy (ARPES) below T_S, which does not fit a simple ferro-orbital order [11, 32, 33].

Having established the presence of critical charge nematic fluctuations, we proceed to show that the struc-

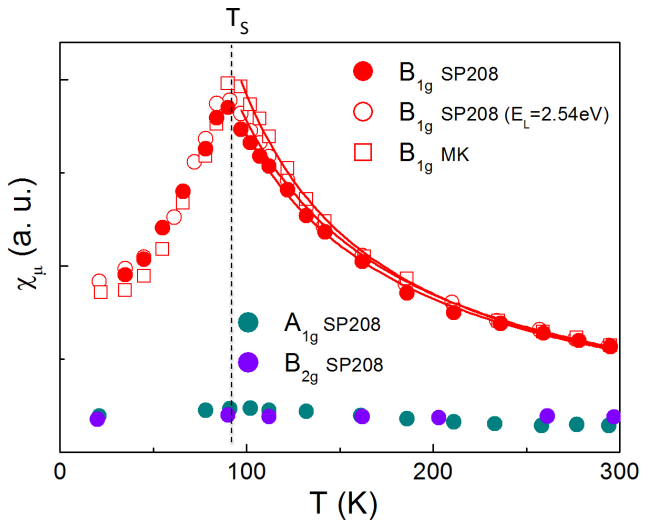

FIG. 3: Temperature dependence of the B_{1g} charge nematic susceptibility for SP208 (T_S=87 K) and MK (T_S=88.5 K) using 2.33 eV photons. Also shown are data on SP208 using a different excitation energy (2.54 eV) and the susceptibility in the other symmetry channels on SP208 (A_{1g} and B_{2g}). The lines are Curie-Weiss fits of the B_{1g} susceptibility above T_S.

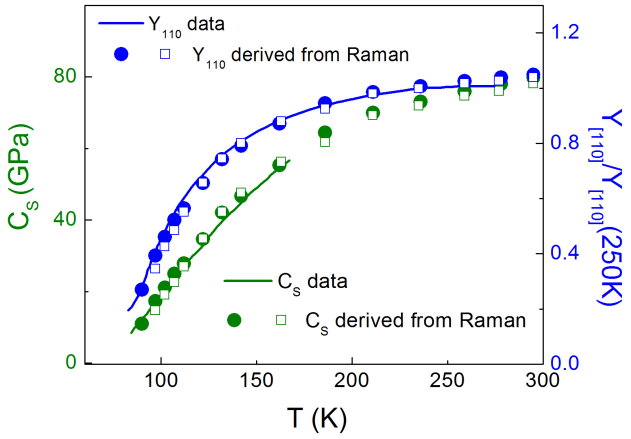

FIG. 4: Shear modulus C_S [10] and Young's modulus $Y_{[110]}$ [8] data (line) and corresponding simultaneous fits using the nematic susceptibility $\chi_{B_{1g}}$ extracted from Raman scattering using eq. 1 and 3. Full / open symbols correspond to Raman data on SP208 / MK crystal. The λ values (in relative units) used for the two crystals agree within 10 percent. The standard relationship between $Y_{[110]}$ and C_S was used [8] (see Supplements for details).

tural instability at T_S is entirely driven by the reported charge nematic softening. The renormalization of the relevant shear modulus C_S due to the above-mentioned symmetry-allowed electron-lattice coupling is given by [6, 8]

$$C_S(T) = C_S^0 - \lambda^2 \chi_{B_{1g}}(T), \qquad (3)$$

We take C_S^0, the bare modulus, to be T-independent as expected for a purely electronic driven structural transition thus leaving λ as the only free parameter. As shown in Fig. 4, we find an excellent agreement between the observed softening of C_S, obtained either directly from ultra-sound measurements [10], or indirectly from Young's modulus measurements [8], and $\chi_{B_{1g}}(T)$ obtained from our Raman measurements. Together with the absence of scaling between elastic modulus and spin fluctuations, our result makes a strong case for a lattice distortion in FeSe induced by a d-wave Pomeranchuk instability of the Fermi surface.

Next, we discuss the frequency dependence of the B_{1g} response in the tetragonal phase. As is evident from the spectra close to T_S in Fig. 2(a), the B_{1g} response is composed of two contributions, a sharp quasi-elastic peak (QEP) at low energy (below 200 cm^{-1}), and a much broader peak centered around 400 cm^{-1}. Both features appear only in the B_{1g} symmetry: $\chi''_{B_{1g}}(\omega) = \chi''_{QEP}(\omega) + \chi''_b(\omega)$. The low energy QEP is well reproduced by a damped Lorentzian $\chi''_{QEP}(\omega) = A_1 \frac{\omega\Gamma}{\omega^2+\Gamma^2}$, which allows a clear separation of the two contributions, and the extraction of the broad $\chi''_b(\omega)$ close to T_S (see Fig. 5(a) and Supplements). As shown in Fig. 5(b), their respective contributions $A_1(T)$ and $A_2(T)$ to the nematic susceptibility $\chi_{B_{1g}}(T)$, through Eq. (1), have different behavior close to T_S in the tetragonal phase. Only the QEP contribution is critical, with $A_1(T)^{-1}$ extrapolating to zero close to T_0. In contrast, the broad peak contribution $A_2(T)$, while sizable, increases only mildly upon cooling. In addition, the extracted QEP line width $\Gamma(T)$ shows a strong softening and extrapolates to zero at ∼65 K (Fig. 5(c)).

In a weak coupling description of a d-wave Pomeranchuk instability, the QEP can be understood as the standard Drude contribution to the Raman conductivity $\chi''_{B_{1g}}(\omega)/\omega$ with weight A_1 and width Γ that are renormalized by the diverging nematic correlation length ξ [6]. Defining $r_0 \equiv \xi^{-2} \propto (T - T_0)$, this theory predicts $A_1^{-1} \propto r_0$, and $\Gamma \propto \Gamma_0 r_0$, where Γ_0 is a single particle scattering rate. As shown in Fig. 5 (b) and (c), the linear temperature dependencies of A_1^{-1} and Γ between T_S and T_S+60 K are in agreement with the above expectation. However, the two quantities extrapolate to zero at different temperatures 20 K (± 10 K) and at 65 K (± 5 K) respectively. We attribute this mismatch to a strong linear temperature dependence of the scattering rate $\Gamma_0(T)$, as suggested by resistivity measurements [1, 2] (see Supplements).

Finally we discuss the microscopic origin of the broad feature. It is unlikely to be from an Azlamazov-Larkin type contribution of the fluctuations of the stripe magnetic state [7, 24, 37, 38] because, below T_S, inelastic neutron scattering and NMR data suggest an enhancement of low energy spin fluctuations [4, 8, 14], whereas we observe a shift of spectral weight of $\chi''_b(\omega)$ to higher

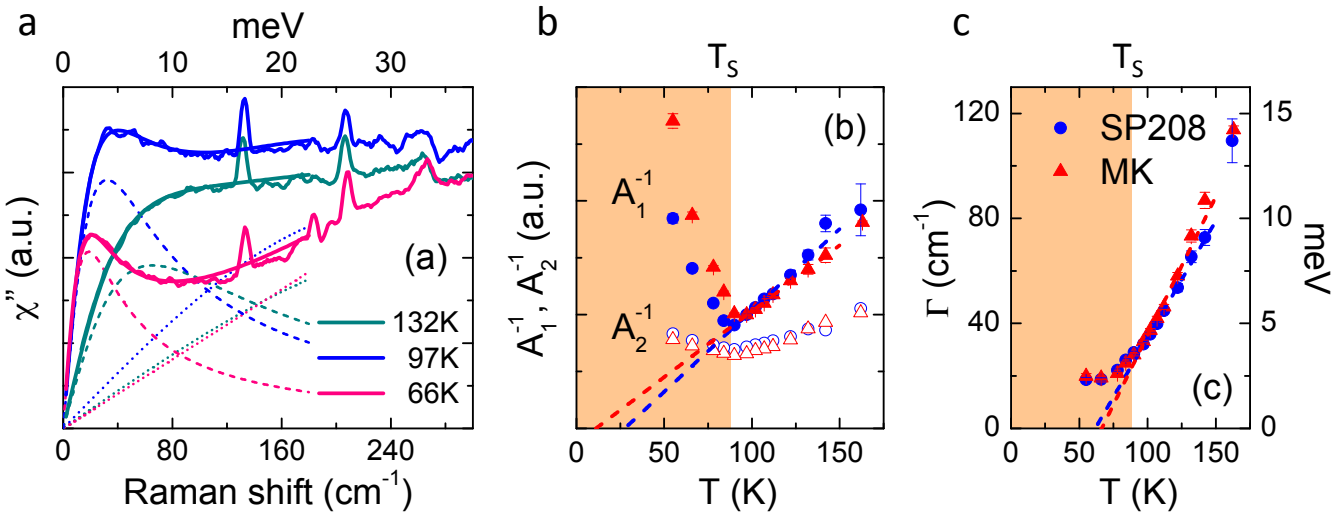

FIG. 5: (a) Low energy fits of the B_{1g} response of SP208 using a damped Lorentzian for the quasi-elastic peak (QEP) and an odd in frequency third order polynomial for the low energy part of the broad peak (see Supplements) . (b) Temperature dependence of the inverse of the two contributions to the nematic susceptibility, A_1^{-1} and A_2^{-1} for SP208 (blue dots) and MK (red triangle). The dashed line is a linear fit of A_1^{-1} between T_S and 150 K. (c) Temperature dependence of the QEP line width Γ_1. The dashed line is a linear fit between T_S and 150 K

frequencies. It is also unlikely that the feature is an interband transition, since $\chi_b''(\omega)$ does not show any gap at low frequencies above T_S (see Supplements). One possibility is that it is the nematic response of electrons that are not sharply defined quasiparticles. Such an interpretation would be in line with the observed bad metal behavior [2, 13], and the fact that the Fermi energy of FeSe is rather small [2, 11, 12].

Overall, our findings support a scenario in which the nematic transition of FeSe is due to an incipient d-wave Pomeranchuk instability of the Fermi surface. This provides an alternative route to nematicity compared to the prevailing spin fluctuation mediated scenario that has been proposed for other Fe SC. The subsequent challenge will be to identify the microscopic interaction that is responsible for the Pomeranchuk instability, and to study if such an interaction is relevant for other Fe SC as well.

Materials and Methods Single crystals of FeSe were grown using chemical vapor transport method based on the use of an eutectic mixture of AlC_3/KCl as described in [1, 2]. The two different single crystals measured were grown in Grenoble (SP208) and Kyoto (MK). Polarization-resolved Raman experiments have been carried out using a diode-pumped solid state (DPSS) laser emitting at 2.33 eV. For low energy (< 500 cm^{-1}) measurements a triple grating spectrometer equipped with 1800 grooves/mm gratings and a nitrogen cooled CCD camera were used. Measurements at higher energies, up to 2000 cm^{-1}, were performed using a single grating spectrometer with 600 grooves/mm in combination with an ultra-steep edge filter (Semrock) to block the stray-light. Additional measurements were also performed using the 2.54 eV line of an Ar-Kr Laser.

We thank G. Blumberg, V. Brouet, A. V. Chubukov, V. D. Fil, R. Hackl and J. Schmalian for fruitful discussions. P. M., M.A. M., M. C., A. S. and Y. G. acknowledge financial support from ANR Grant "Pnictides", from a Labex SEAM grant and from a SESAME grant from région Ile-de-France. P. T. and S. Karlsson acknowledge the financial support of UJF (now integrated inside "Université Grenoble Alpes") and Grenoble INP through the AGIR-2013 contract of S. Karlsson. S. Kasahara., T. S. and Y. M. acknowledge the support of Grants-in-Aid for Scientific Research (KAKENHI) from Japan Society for the Promotion of Science (JSPS), and the 'Topological Quantum Phenomena' (No. 25103713) Grant-in-Aid for Scientific Research on Innovative Areas from the Ministry of Education, Culture, Sports, Science and Technology (MEXT) of Japan.

* Electronic address: yann.gallais@univ-paris-diderot.fr

[1] J.-H. Chu, et al. (2010) In-Plane Resistivity Anisotropy in an Underdoped Iron Arsenide Superconductor, *S*cience 329:824-826.

[2] R. M. Fernandes, A. V. Chubukov, and J. Schmalian (2014) What drives nematic order in iron-based superconductors? *Nature Physics* 10:97.

[3] T. M. McQueen, et al. (2009) Tetragonal-to-Orthorhombic Structural Phase Transition at 90K in the Superconductor $Fe_{1.01}Se$, *Phys. Rev. Lett.* 103:057002.

[4] T. Imai, et al. (2009) Why Does Undoped FeSe Become A High Tc Superconductor Under Pressure?, *Phys. Rev.*

Lett. 102:177005.
[5] S. -H. Baek, et al. (2014) Orbital-driven nematicity in FeSe, *N*ature Mater. 14:210-214.
[6] A. E. Boehmer, et al. (2015) Origin of the Tetragonal-to-Orthorhombic Phase Transition in FeSe: A Combined Thermodynamic and NMR Study of Nematicity, *Phys. Rev. Lett.* 114:027001.
[7] S. Medvedev, et al. (2009) Electronic and magnetic phase diagram of β-$Fe_{1.01}Se$ with superconductivity at 36.7 K under pressure, *Nature Mater.* 8:630.
[8] G. Garbarino, et al. (2009) High-temperature superconductivity (Tc onset at 34 K) in the high-pressure orthorhombic phase of FeSe, *E*PL 86:27001.
[9] S. Kasahara, et al. (2014) Field-induced superconducting phase of FeSe in the BCS-BEC cross-over, *Proc Natl Acad Sci USA* 46:16309.
[10] T. Terashima, et al. (2014) Anomalous Fermi surface in FeSe seen by Shubnikov-de Haas oscillation measurements, *P*hys. Rev. B 90:144517.
[11] M. D. Watson, et al. (2015) Emergence of the nematic electronic state in FeSe, *P*hys. Rev. B 91:155106.
[12] A. Audouard et al. (2015) Quantum oscillations and upper critical magnetic field of the iron-based superconductor FeSe *E*PL 109:27003.
[13] M. Aichhorn, S. Biermann, T. Miyake, A. Georges, and M. Imada (2010) Theoretical evidence for strong correlations and incoherent metallic state in FeSe, *P*hys. Rev. B 82:064504.
[14] Q. Wang, et al. (2015) Strong interplay between stripe spin fluctuations, nematicity and superconductivity in FeSe, *Nature Mater.* 15:159.
[15] J. K. Glasbrenner, et al. (2015) Effect of magnetic frustration on nematicity and superconductivity in iron chalcogenides, *Nature Phys.* 11:953.
[16] F. Wang, S. Kivelson and D. -H. Lee (2015) Nematicity and quantum paramagnetism in FeSe, *Nature Phys.* 11:959.
[17] A. V. Chubukov, R. M. Fernandes and J. Schmalian (2015) Origin of nematic order in FeSe, *Phys. Rev. B* 91:201105(R).
[18] R. Yu and Q. Si (2015) Antiferroquadrupolar and Ising-Nematic Orders of a Frustrated Bilinear-Biquadratic Heisenberg Model and Implications for the Magnetism of FeSe *Phys. Rev. Lett.* 115:116401.
[19] Y. Yamakawa, S. Omari and H. Kontani (2016) Nematicity and Magnetism in FeSe and Other Families of Fe-Based Superconductors, *Phys. Rev. X* 6:021032.
[20] K. Jiang, J.-P. Hu, H. Ding and Z. Wang (2016) Interatomic Coulomb Interaction and Electron Nematic Bond Order in FeSe *Phys. Rev. B* 93:115138.
[21] Y. Su, H. Liao, and T. Li (2015) The form and origin of orbital ordering in the electronic nematic phase of iron-based superconductors, *J. Phys. Condens. Matter* 27:105702.
[22] H. Yamase and R. Zeyher (2013) Electronic Raman scattering from orbital nematic fluctuations *Phys. Rev. B* 88:125120.
[23] Y. Gallais, et al. (2013) Observation of Incipient Charge Nematicity in Ba(Fe1-xCox)2As2 *Phys. Rev. Lett.* 111:267001.
[24] H. Kontani and Y. Yamakawa (2014) Linear Response Theory for Shear Modulus C66 and Raman Quadrupole Susceptibility: Evidence for Nematic Orbital Fluctuations in Fe-based Superconductors *Phys. Rev. Lett.* 113:047001.
[25] Y. Gallais and I. Paul (2016) Charge nematicity and electronic Raman scattering in iron-based superconductors, *C. R. Physique* 17:113-139.
[26] V. K. Thorsmølle, et al. (2016) Critical Charge Fluctuations in Iron Pnictide Superconductors, *Phys. Rev. B* 93:054515.
[27] F. Kretzschmar, et al. (2016) Critical spin fluctuations and the origin of nematic order in Ba(Fe1-xCox)2As2, *Nature Phys.* 12:560-563.
[28] I. J. Pomeranchuk (1958) On the stability of a Fermi liquid, *Sov. Phys. JETP* 8:361.
[29] G. A. Zvyagina, et al. (2013) Acoustic characteristics of FeSe single crystals, *E*PL 101:56005.
[30] T. P. Devereaux and R. Hackl (2007) Inelastic light scattering from correlated electrons, *Rev. Mod. Phys.* 79:175.
[31] S. Karlsson, et al. (2015) Study of high-quality superconducting FeSe single crystals: crossover in electronic transport from a metallic to an activated regime above 350 K, *Supercond. Sci. Technol.* 28:105009.
[32] Y. Suzuki, et al. (2015) Momentum-Dependent Sign-Inversion of Orbital Polarization in Superconducting FeSe, *Phys. Rev. B* 92:205117.
[33] P. Zhang, et al. (2015) Observation of Two Distinct dxz=dyz Band Splittings in FeSe, *Phys. Rev. B* 91:214503.
[34] V. Gnezdilov, et al. (2013) Interplay between lattice and spin states degree of freedom in the FeSe superconductor: Dynamic spin state instabilities, *Phys. Rev. B* 87:144508.
[35] Y. Gallais, I. Paul, L. Chauvière and J. Schmalian (2016) Nematic resonance in the Raman spectrum of iron-based superconductors *Phys. Rev. Lett.* 116:017001.
[36] A. V. Chubukov, M. Khodas and R. M. Fernandes (2016) Magnetism, superconductivity, and spontaneous orbital order in iron-based superconductors: who comes first and why? arXiv:1602.05503
[37] M. Khodas and A. Levchenko (2015) Raman scattering as a probe of nematic correlations, *Phys. Rev. B* 91:235119.
[38] U. Karahasanovic et al. (2015) Manifestation of Nematic Degrees of Freedom in the Raman Response Function of Iron Pnictides *Phys. Rev. B* 92:075134.
[39] A. A. Maksimov, *et al.* (1992) Investigations of the temperature dependence of the low energy electronic Raman scattering in Ti2Ba2CaCu2O8 single crystals *Solid State Comm.* 81:407.
[40] M. Yoshizawa, *et al.* (2012) Structural Quantum Criticality and Superconductivity in Iron-Based Superconductor Ba(Fe1 xCox)2As2, *J. Phys. Soc. Jpn* 81:024604.
[41] S. Simayi et al. (2013) Strange Inter-layer Properties of Ba(Fe1-xCox)2As2 Appearing in Ultrasonic Measurements, arXiv:1310.2681
[42] S. Chandra and A. K. M. A. Islam (2010) Elastic properties of mono- and poly-crystalline PbO-type FeSe1-xTex (x = 0-1.0): A first-principles study, *Physica C* 470:2072.

Supplementary Information for "Charge induced nematicity in FeSe"

I. METHODS

Single crystals of FeSe were grown using chemical vapor transport method based on the use of an eutectic mixture of AlC_3/KCl as described in [1, 2]. The two different single crystals measured were grown in Grenoble (SP208) and Kyoto (MK). The structural transition temperatures were determined in-situ by monitoring the emergence of Rayleigh scattering by orthorhombic domains yielding T_S=87 K and T_S=88.5 K for SP208 and MK respectively (see below for details). These values are in agreement with T_S values extracted from transport measurement (see Fig. 14(a) and [1, 2].) The superconducting transition temperatures T_c were measured using SQUID magnetometry giving T_c=8.5 K (SP208) and T_c=9.1 K (MK). Again, these T_c values confirm the values extracted from transport measurements (see Fig. 14(a) and [1, 2]). The crystals were cleaved and transferred to a close-cycle cryostat in inert atmosphere to prevent surface degradation.

Polarization-resolved Raman experiments have been carried out using a diode-pumped solid state (DPSS) laser emitting at 2.33 eV. For low energy (< 500 cm^{-1}) measurements a triple grating spectrometer equipped with 1800 grooves/mm gratings and a nitrogen cooled CCD camera were used. Measurements at higher energies, up to 2000 cm^{-1}, were performed using a single grating spectrometer with 600 grooves/mm in combination with an ultra-steep edge filter (Semrock) to block the stray-light. Additional measurements were also performed using the 2.54 eV line of an Ar-Kr Laser. The laser spot dimension was $\sim$ 50x80 μm^2. The typical laser power used was 8 mW, but for spectra in the superconducting state laser power less than 0.2 mW was used. All temperatures were corrected for the estimated laser heating (see below for details).

The B_{1g} and B_{2g} symmetries were obtained using perpendicular incoming and outgoing photon polarizations at 45 degrees, and along of the Fe-Fe bonds respectively. When using parallel incoming and outgoing photon polarizations at 45 degrees of the Fe-Fe bonds, A_{1g} + B_{2g} symmetries are probed. The A_{1g} component can be isolated from the A_{1g}+B_{2g} spectra by subtracting the B_{2g} contribution obtained independently. A piezo-rotator was used to change the orientation of the crystal in-situ with respect to the photon polarizations. In order to extract the symmetry dependent nematic susceptibility from the Raman response at finite frequency using Kramers-Kronig relation, the responses were extrapolated linearly from the lowest frequency measured (8 - 9 cm^{-1} depending on the symmetry and sample) to zero frequency.

II. LASER HEATING AND DETERMINATION OF T_S

A clear manifestation of the structural transition is the appearance of Rayleigh scattering at the surface of the crystal due to twin domains formation at $T_{\rm S}$. This effect is easy to monitor using a camera to visualize the laser spot during Raman experiments. Moreover, it is very useful to estimate the actual value of $T_{\rm S}$, as well as laser heating in-situ.

To achieve this, we take pictures of the laser spot at different temperatures for a given value of laser power $P_{\rm L}$ (see figure 6), then integrate out the whole spot intensity and plot it as a function of temperature (see figure 7).

Figure 6 shows images of the laser spot taken at different temperatures on the SP208 sample, for a laser power of 0.5 mW. These images show the onset of twin domains scattering at a temperature $T_{\rm DS}$ between 87.5 K and 87.0 K. Since twin domains scattering appears when the effective temperature equals $T_{\rm S}$, the onset temperature $T_{\rm DS}$ depends on the value of laser heating.

Figure 7 shows the temperature dependence of the integrated intensity on SP208 at a laser power of 0.5 mW. It shows an order parameter-like behaviour, which extrapolates at a temperature $T^{\rm off}_{\rm DS,1} = 86.5$ K. Note that the integrated intensity starts to be non-zero at a temperature slightly above $T^{\rm on}_{\rm DS,1} = 87.5$ K. This behavior may be due to either the gaussian tail of the laser spot, for which the actual laser heating is lower than that measured at the center of the laser spot, or to a slightly inhomogeneous distribution of $T_{\rm S}$.

The same measurement was also performed for a higher laser power of 5 mW. The order parameter fit gives $T^{\rm off}_{\rm DS,2} = 82.6$ K. Assuming the following linear relation between the three quantities $T_{\rm S}$, $T^{\rm off}_{\rm DS}$ and $H_{\rm L}(T_{\rm S})$:

$$T_{\rm S} = T^{\rm off}_{\rm DS} + H_{\rm L}(T_{\rm S}) \times P_{\rm L}$$

we can thus determine the actual $T_{\rm S}$ of our sample and the laser heating at transition $H_{\rm L}(T_{\rm S})$. We deduce from our two measurements :

$$\{\, T_{\rm S} = 86.9 \pm 0.4\,{\rm K} H_{\rm L}(T_{\rm S}) = 0.9\,{\rm K/mW}$$

The same procedure was applied to sample MK yielding, within error bars, the same estimation of laser heating, but a slightly higher T_S: T_S=88.5 $\pm$0.5 K. Knowing these quantities and the temperature dependence of thermal conductivity $\kappa(T)$, we can compute an estimation of laser heating as a function of temperature $H_{\rm L}(T)$ using the method described in ref [3].

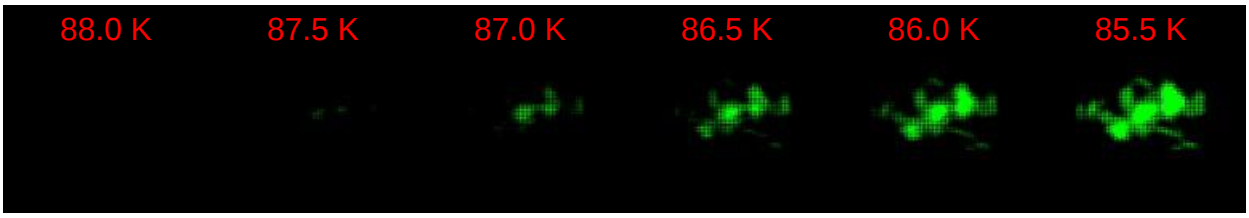

FIG. 6: Images of the laser spot at different temperatures, taken on an SP208 sample, for a laser power of 0.5 mW.

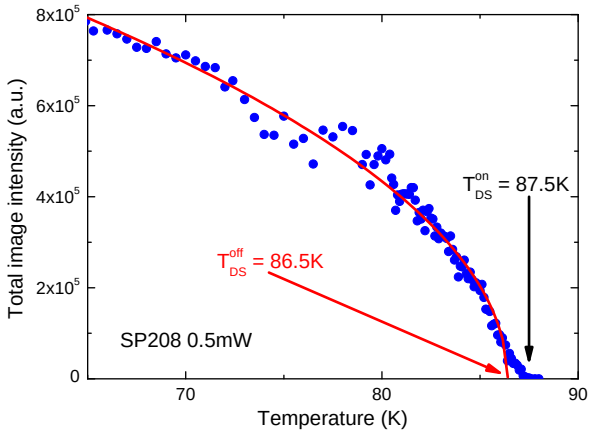

FIG. 7: Integrated laser spot image intensity as a function of temperature, for sample SP208, at a laser power of 0.5 mW.

III. COMPARISON WITH CO-BA122

While there is an apparent contrast between FeSe and other Fe SC with respect to spin degrees of freedom we show in figure 8(a) that, when plotted as a function of T-T_0, the temperature dependence of the charge nematic susceptibility of FeSe is remarkably similar to the one of electron doped Co-Ba122 [5]. However the two systems differ in the magnitude of the splitting between T_S and T_0, which in a simple Landau-type picture measures the strength of the electron-lattice coupling [4]. The splitting is 70-80 K for FeSe while it is less than 60 K in Co-Ba122 (40 K for undoped Ba122) indicating a larger electron-lattice coupling energy in FeSe (Fig. 8(b)).

IV. LINK BETWEEN C_S, $Y_{[110]}$ AND NEMATIC SUSCEPTIBILITY

Here we give details on the link between the Raman charge nematic susceptibility, the shear modulus and Young's modulus along the [110] direction, as measured in 3-point bending measurements [8].

A. Link between C_S and $Y_{[110]}$

According to elasticity theory $Y_{[110]}$ can be expressed as a function of the components of the elastic tensor as:

$$Y_{[110]} = 4[\frac{1}{C_S} + \frac{1}{\gamma}]^{-1} \tag{4}$$

Using the Voigt notation and the tetragonal (2 Fe) unit cell, the shear modulus is given by C_S=C_{66}. The coefficient γ depends on four other components: $\gamma = \frac{C_{11}}{2} + \frac{C_{12}}{2} + \frac{C_{13}^2}{C_{33}}$. As in all Fe SC, C_S is the only soft component above T_S. The other components have a weak temperature dependence due to anharmonicity and can be safely approximated as constants between 300K and T_S [9, 10]. Sufficiently close to T_S the behavior of $Y_{[110]}$ will therefore be dominated by C_S which strongly softens: $\frac{Y_{[110]}}{Y^0_{[110]}} \approx \frac{C_S}{C^0_S}$. However this approximation holds only very close T_S, and far away from T_S the proportionality between the 2 quantities will not be verified. This can be illustrated by assuming that C_S follows a Curie-Weiss dependence as observed in Co-Ba122:

$$C_S = C^0_S \frac{T - T_S}{T - T_0} \tag{5}$$

T_S is the structural transition temperature and T_0 can be thought as the electronic nematic transition temperature in the absence of coupling to the lattice. T_0 can be identified as the Curie-Weiss temperature extracted from Raman measurements if only charge and lattice degrees of freedom are considered. It is straightforward to compute the corresponding temperature dependence of $Y_{[110]}$:

$$Y_{[110]} = \frac{4C^0_S}{1+\alpha} \frac{T - T_S}{T - T_1} \tag{6}$$

where $\alpha = \frac{C^0_S}{\gamma}$ and

$$T_1 = \frac{T_0 + \alpha T_S}{1 + \alpha} \tag{7}$$

The temperature dependence of $Y_{[110]}$ is still of Curie-Weiss type but with a new characteristic temperature $T_1 \neq T_0$. In the limit where $\alpha << 1$ we have $T_1 \approx T_0$. This limit is however never reached in Fe SC where

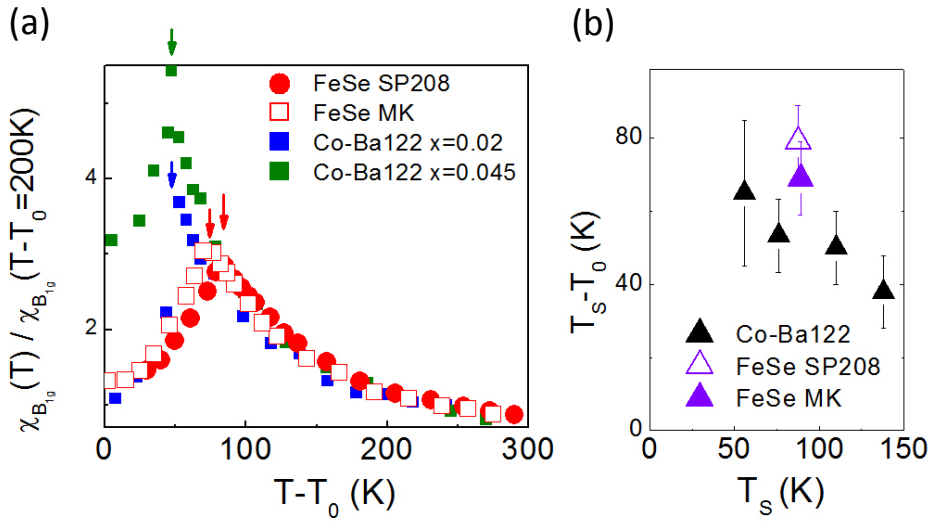

FIG. 8: (a) Comparison between the B_{1g} charge nematic susceptibility of FeSe and Co doped $BaFe_2As_2$ [5] plotted as a function of T-T_0 where T_0 is the Curie-Weiss temperature of each sample. The arrows indicate the structural transition T_S for each sample. (b) Electron-lattice coupling energy T_S-T_0 as a function of T_S for FeSe and Co-Ba122.

α ≈0.7 in Ba122 and α ≈=1.5 in FeSe. In general T_1 will be bounded by T_0 from below, and T_S from above: $T_0 < T_1 < T_S$. The disagreement between C_S and its estimate from $Y_{[110]}$ will therefore be marginal when T_0 and T_S are close like in Ba122 (about 40 K). However in FeSe where $T_S - T_0 \sim 70\ K$ the difference is more significant, and the full expression 4 must be used. This is illustrated in fig. 9 (a) and (b) where the normalized temperature dependences of C_S and $Y_{[110]}$ are plotted for parameters relevant to Ba122 and FeSe respectively.

B. Simultaneous scaling of C_S and $Y_{[110]}$ with $\chi_{B_{1g}}$

The comparison between the experimentally observed softening of C_s and the one expected from the charge nematic susceptibility $\chi_{B_{1g}}$ was performed using equation 2 of the main text with C_s^0=105 (110) GPa for SP208 (MK) sample. The only free parameter was the electron-lattice coupling λ and good agreement was found for each sample in the temperature interval where C_S was measured. The λ value used for SP208 was 10% higher than for MK. Note that since $\chi_{B_{1g}}$ extracted from Raman measurements is only known in relative units, we cannot access the absolute value of λ from the fits. Using the same parameters, C_S^0 and λ, the associated softening of $Y_{[110]}$ was then computed using equation 4 with γ=70 GPa, as estimated from both elastic constant measurements and ab-initio calculations [10, 11]. As $Y_{[110]}$ is only known up to a constant prefactor, the data were rescaled at 250 K [8].

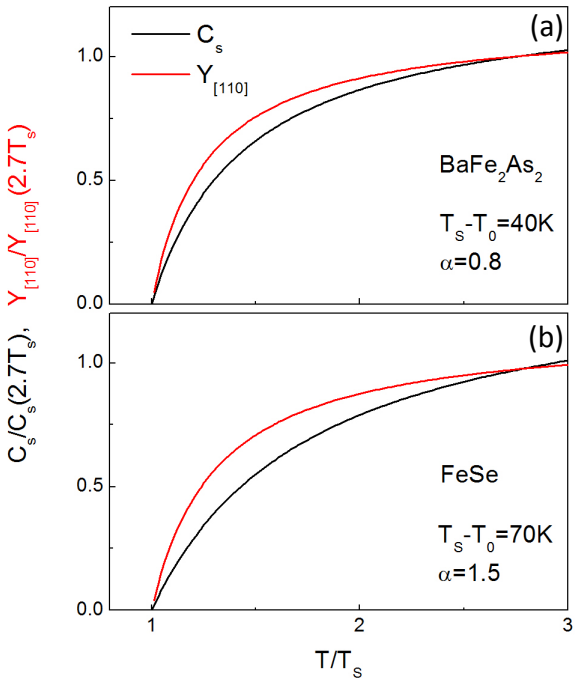

FIG. 9: Theoretical Curie-Weiss temperature dependences of C_S and $Y_{[110]}$ for different value of $T_S - T_0$ and α. (a) corresponds to parameters relevant for $BaFe_2As_2$ and (b) for FeSe. Values were rescaled at T=2.7T_S.

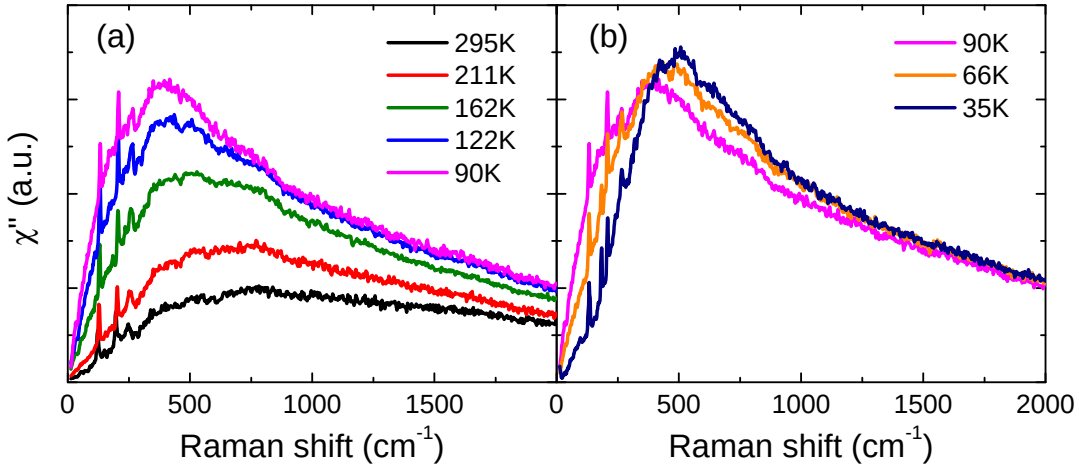

FIG. 10: High energy contribution to the B_{1g} Raman response, with the low energy QEP component subtracted, of sample SP208 at 2.33 eV (532 nm) as a function of temperature (a) above T_S and (b) below T_S.

V. FITTING PROCEDURE OF THE FINITE FREQUENCY B_{1g} RESPONSE

A. Fits using a quasi-elastic peak and a low energy background

In order to quantify the temperature dependences of the two components contributing to nematic fluctuations in FeSe, it is necessary to fit Raman response data, especially the low-energy Quasi-Elastic Peak (QEP). To achieve this, we used the following general expression :

$$\chi^{''}(\omega,T) = \chi^{''}_{\rm QEP}(\omega,T) + \chi''_b(\omega,T) \qquad (8)$$

where the QEP is modeled by an damped Lorentzian:

$$\chi^{''}_{\rm QEP}(\omega,T) = A_1(T)\frac{\Gamma(T)\omega}{\omega^2+\Gamma^2(T)} \qquad (9)$$

At low energy the broad peak χ''_b was modeled using a third order polynomial form with only odd powers in ω to guaranty causality.

$$\chi''_b(\omega,T) = b_1(T)\omega + b_3(T)\omega^3 \qquad (10)$$

As is clear from figure 4(a) of the main text and from figures 11(a) and 12(a), equation (8) fits well the Raman response data at low energy, up to at least 180 cm^{-1}, and at all temperatures, above and below T_S. In particular, below T_S, the high energy peak is partially gapped (see also figure 10), resulting in a change in parameter $b_3(T)$ from negative values above T_S to positive values deep below T_S.

Figures 4(b) of the main text and 11(b) and 12(b) show the temperature dependences of the inverse of the two contributions to the nematic susceptibility, A_1 and A_2. The temperature dependences $A_1(T)$ for all samples were fitted between 95 K and 150 K using a linear form $A_1(T) = a_1.(T - T^*)$. $A_2(T)$ was computed using the following method : the low energy QEP fits were subtracted from the full Raman responses (Fig. 10). The spectra were then divided by frequency and integrated up to 2000 cm^{-1}.

Figures 4(c) of the main text and 11(c) and 12(c) show the temperature dependences of the line width Γ of the QEP, directly extracted from fits of the Raman response using equation (8). The temperature dependences $\Gamma(T)$ were fitted between 95 K and 150 K using a linear form $\Gamma(T) = \Gamma_0(T - T^{**})$.

B. Fits using two quasi-elastic peaks

As shown in figure 13(a), we found that the data can also be well fitted above T_S with a sum of two QEPs, as expected from the contributions of two intraband, Drude-like, terms:

$$\chi^{''}(\omega, T > T_S) = \chi^{''}_{\rm QEP_1}(\omega,T) + \chi^{''}_{\rm QEP_2}(\omega,T) \qquad (11)$$

where

$$\chi^{''}_{\rm QEP_{1,2}}(\omega,T) = A_{1,2}(T).\frac{\Gamma_{1,2}(T)\omega}{\omega^2+\Gamma^2_{1,2}(T)} \qquad (12)$$

Fits using equation (11) are good up to 1000 cm^{-1}, strengthening our interpretation that the brand peak arises from more incoherent intraband excitations. Note however, that because of the partial gapping mentioned above, the two QEP analysis does not reproduce the data satisfactorily below T_S. Figure 13(b) shows the temperature dependences of the inverse of the two contributions to the nematic susceptibility, A_1 and A_2 extracted

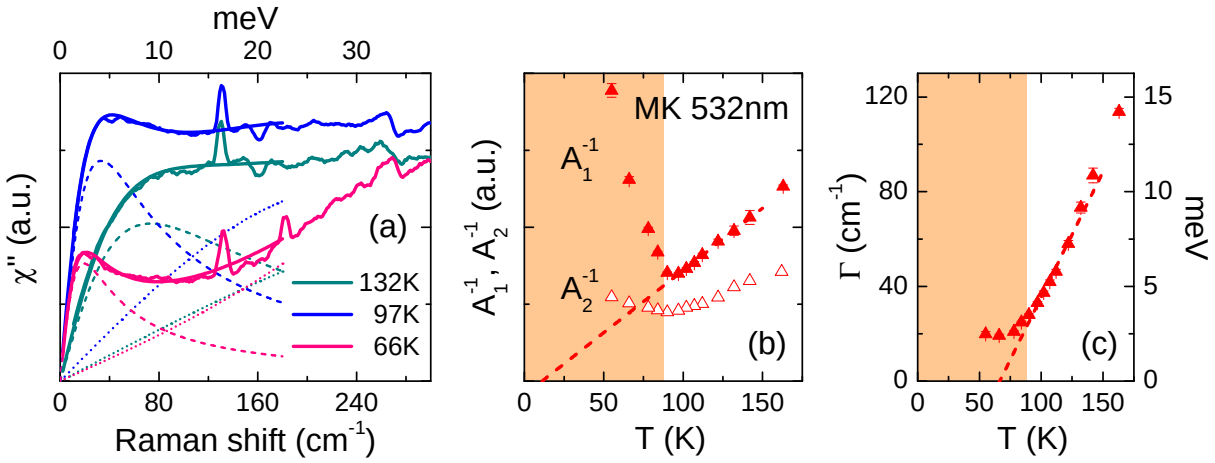

FIG. 11: (a) Low energy fits of the B_{1g} response of sample MK at 2.33 eV (532 nm) using equation (8). (b) Temperature dependences of the inverse of the two contributions to the nematic susceptibility, A_1 and A_2 (red triangles, same as in figure 4 of the main text). The dashed line is a linear fit of A_1^{-1} between T_S and 150 K. It crosses the x-axis at $T^* = 11$ K. (c) Temperature dependence of the line width Γ of the QEP. The dashed line is a linear fit between T_S and 150 K. It crosses the x-axis at $T^{**} = 66$ K.

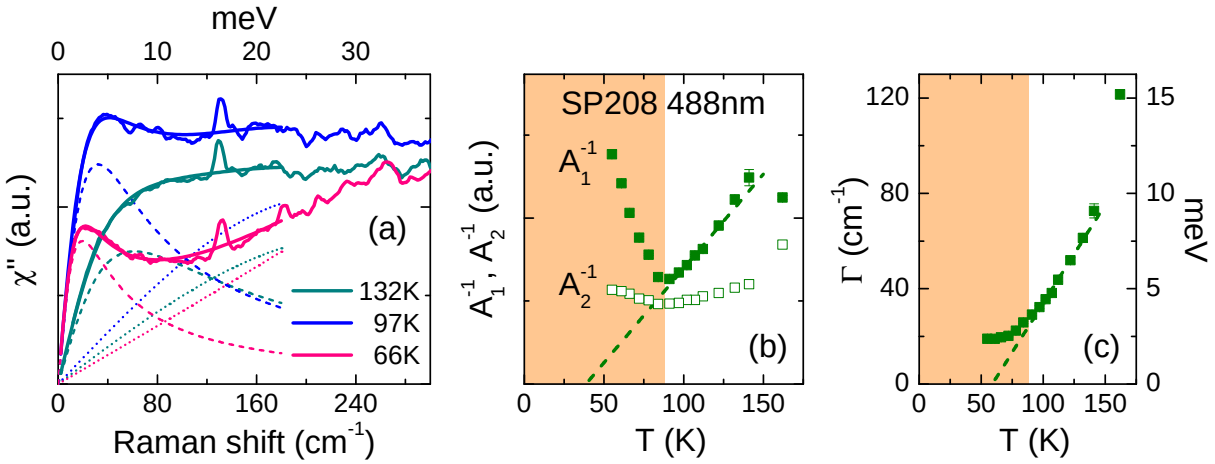

FIG. 12: (a) Low energy fits of the B_{1g} response of sample SP208 at 2.54 eV (488 nm) using equation (8). (b) Temperature dependences of the inverse of the two contributions to the nematic susceptibility, A_1 and A_2. The dashed line is a linear fit of A_1^{-1} between T_S and 150 K. It crosses the x-axis at $T^* = 39$ K. (c) Temperature dependence of the line width Γ of the QEP. The dashed line is a linear fit between T_S and 150 K. It crosses the x-axis at $T^{**} = 59$ K.

from the fits. Figure 13(c) shows the temperature dependences of the line widths Γ_1 and Γ_2 of QEP_1 and QEP_2, respectively. Both quantities show linear temperature dependences, indicated by dashed and dotted lines, respectively.

VI. QEP LINE WIDTH AND RESISTIVITY

In a Random Phase Approximation picture of a d-wave Pomeranchuk transition we expect the QEP amplitude $A_1^{-1}(T)$ to scale as $r_0(T)$. Here $r_0(T) = \xi^{-2} \propto T - T_0$, where $\xi(T)$ is the nematic correlation length and T_0 the mean-field nematic transition temperature [6]. Experimentally T^*, the zero temperature intercept of $A_1^{-1}(T)$ (T^* ∼25 K (± 15 K)), is indeed close to T_0, as obtained from the global Curie-Weiss fit of $\chi_{B_{1g}}$. However the zero temperature intercept of the QEP line width Γ, T^{**}, is significantly higher: $T^{**} \sim 65$ K (±5 K).

Here we show that the shift between T^* and T^{**} can be accounted by the temperature dependence of the bare quasiparticle scattering $\Gamma_0(T)$ as measured by e.g. transport. In FeSe, and in contrast to e.g. $BaFe_2As_2$, the resistivity is strongly temperature dependent above T_S. Between T_S and 200 K it show quasi-linear behavior with a positive intercept on the temperature axis. Since $\Gamma(T) \propto \Gamma_0(\mathrm{T})\ r_0(T)$, the temperature dependence of the QEP line width Γ will contain contributions coming from both the quasiparticle scattering rate $\Gamma_0(T)$ and $r_0(T)$.

Assuming that $\Gamma_0(T)$ is proportional to the resistivity, $\Gamma_0 \propto R$, we can extract the temperature dependence of $r_0(\mathrm{T})$ by dividing the measurement of QEP line width Γ by the resistance R:

$$\frac{\Gamma(T)}{R(T)} \propto r_0(T) \tag{13}$$

We have used the resistivity data on a crystal from the same batch as SP208 (fig. 14) to correct the temperature dependence of $\Gamma(\mathrm{T})$. $\Gamma(\mathrm{T})$ and $\frac{\Gamma(T)}{R(T)}$, normalized at their 160 K values, are shown in Fig. 14(b). While the temperature dependence of $\Gamma(\mathrm{T})$ between T_S and 150 K extrapolates linearly at T^{**} ∼65 K, the quantity $\frac{\Gamma(T)}{R(T)}$ extrapolates at a lower temperature ∼ 15 K, now much closer to the value of T^* extracted from the temperature dependence of QEP amplitude A_1^{-1}. Taking into account the temperature dependence of the scattering rate $\Gamma_0(T)$ thus reconciles the temperature dependences of $A_1(\mathrm{T})$ and $\Gamma(\mathrm{T})$.

* Electronic address: yann.gallais@univ-paris-diderot.fr

[1] S. Karlsson et al. Supercond. Sci. Technol. 28, 105009 (2015).

[2] S. Kasahara et al. Proc. Nat. Acad. Sci. 111, 16309 (2014)

[3] A. A. Maksimov *et al.*, Solid State Comm. **81** (5), 407 (1992)

[4] M. Yoshizawa, *et al.*, J. Phys. Soc. Jpn **81**, 024604 (2012).

[5] Y. Gallais, R. M. Fernandes, I. Paul, L. Chauvière, Y.-X. Yang, M.-A. Méasson, M. Cazayous, A. Sacuto, D. Colson, and A. Forget, Phys. Rev. Lett. **111**, 267001 (2013).

[6] Y. Gallais and I. Paul, C. R. Physique 17, 113-139 (2016)

[7] F. Kretzschmar et al. Nat. Phys. (2016)

[8] A. E. Boehmer, T. Arai, F. Hardy, T. Attori, T. Iye, T. Wolf, H. v. Lohneysen, K. Ishida and C. Meingast, Phys. Rev. Lett. **114**, 027001 (2015)

[9] S. Simayi et al. arXiv:1310.2681 (2013)

[10] G. A. Zvyagina, T. N. Gaydamak, K. R. Zhekov, I. V. Bilich, V. D. Fil, D. A. Chareev and A. N. Vasilyev, EPL **101**, 56005 (2013)

[11] S. Chandra and A. K. M. A. Islam, Physica C **470**, 2072 (2010)

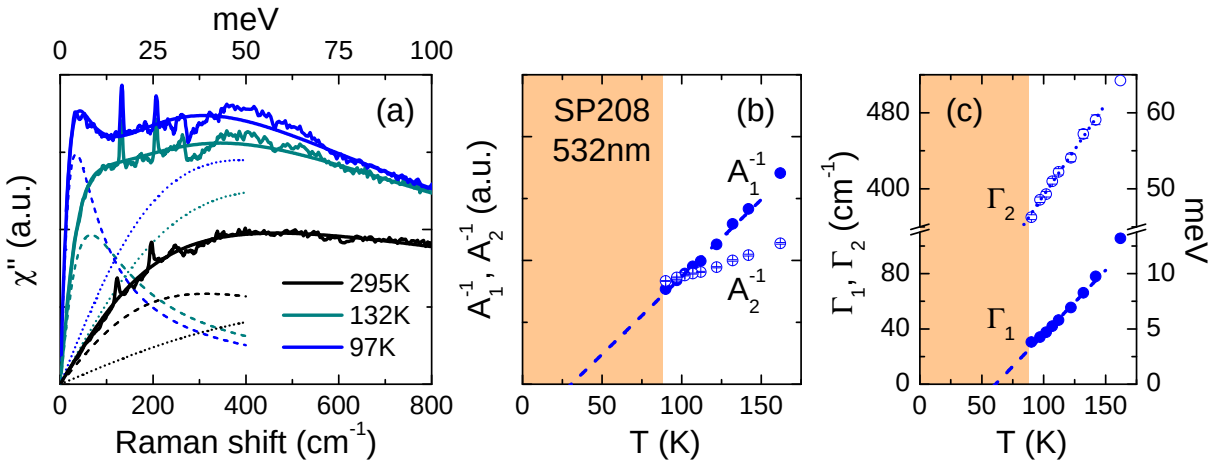

FIG. 13: (a) Low energy fits of the B_{1g} response of sample SP208 at 2.33 eV (532 nm) using equation (11). Note that the energy range is wider than that of figures 4(a), 11(a) and 12(a). (b) Temperature dependences of the inverse of the two contributions to the nematic susceptibility, A_1 and A_2. The dashed line is a linear fit of A_1^{-1} between T_S and 150 K. It crosses the x-axis at $T^* = 31$ K. (c) Temperature dependences of the line widths Γ_1 and Γ_2 of the low and high energy QEPs, respectively. The dashed and dotted lines are linear fits between T_S and 150 K. The dashed line crosses the x-axis at $T^{**} = 61$ K.

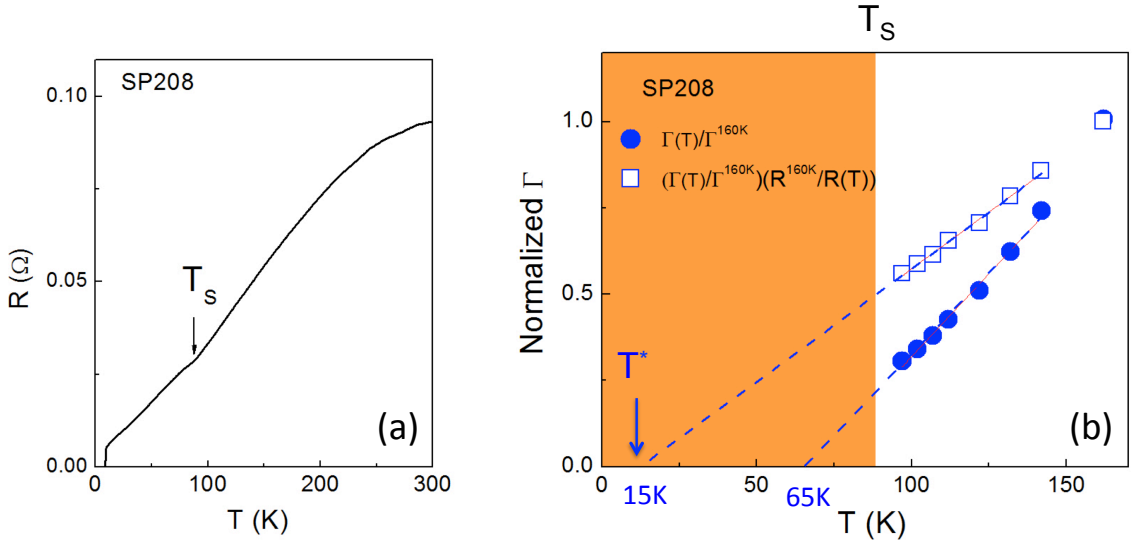

FIG. 14: (a) Temperature dependence of the resistance R of FeSe SP208. (b) Temperature dependence of Γ(T) and $\frac{\Gamma(T)}{R(T)}$, normalized at their 160 K values on FeSe SP208